Composite Structures 152 (2016) 729–736

Contents lists available at ScienceDirect

Composite Structures

journal homepage: www.elsevier.com/locate/compstruct

Bending and benchmark of zero Poisson's ratio cellular structures

Jian Huang [a,c], Qiuhua Zhang [a], Fabrizio Scarpa [b,*], Yanju Liu [a], Jinsong Leng [c,*]

[a] Department of Aerospace Science and Mechanics, No. 92 West Dazhi Street, Harbin Institute of Technology (HIT), P.O. Box 301, Harbin 150080, PR China
[b] Advanced Composites Center for Innovation and Science, University of Bristol, Bristol BS8 1TR, UK
[c] Center for Composite Materials and Structures, No. 2 Yikuang Street, Science Park of Harbin Institute of Technology (HIT), P.O. Box 301, Harbin, PR China

ARTICLE INFO

Article history:
Received 2 May 2016
Accepted 23 May 2016
Available online 25 May 2016

Keywords:
Honeycomb
Mechanical properties
Zero Poisson's ratio
Mechanical testing
Morphing

ABSTRACT

This work describes the bending performance of a zero Poisson's ratio (ZPR) cellular structure made from the tessellation of hexagons and thin plates. This particular ZPR configuration allows achieving large out-of-plane deformations and tailored in-plane and out-of-plane mechanical properties. We present a series of analytical models, finite element simulations and experimental tests to evaluate the bending capability of these cellular structures. A comparison of the out-of-plane bending behavior of six different types of cellular topologies with the same relative density of the ZPR honeycomb has also been carried out by using three-point bending tests. Further parametric analyses have also been performed to determine the dependence of the equivalent bending modulus versus the geometric parameters that define the ZPR honeycomb. The novel ZPR lattices show the highest bending compliance at large strains, and highly tailorable mechanical properties for the design of composite structures for airframe morphing applications.

1. Introduction

Honeycomb structures have attracted considerable attentions as advanced composite materials for their remarkable light-weight and outstanding mechanical properties [1,2]. Different honeycomb configurations achieving zero Poisson's ratio (ZPR), negative Poisson's ratio (NPR) and positive Poisson's ratio (PPR) have been proposed and investigated, with special focus on their in-plane mechanics, flatwise compressive stiffness and the transverse shear stiffness [3–15]. Honeycombs with PPR behavior exhibit anticlastic or saddle-shape curvature when subjected to out-of-plane bending deformation. This feature somehow limits their use in structural applications defined by complex out-of-plane geometry [16–18]. Synclastic curvatures have been observed in the out-of-plane bending deformation of NPR structures [16,19,20]. However, no anticlastic or synclastic curvatures are present in the out-of-plane bending deformation of the cellular structures with ZPR, which makes them more suitable for the use in cylindrical sandwich panels and morphing applications in which the structures need to undergo either one-dimensional (span) morphing or pure cylindrical bending deformation [21,22]. For out-of-plane bending applications one needs to identify the bending deformation mechanisms existing in cellular structures. Abd El-Sayed et al. [23] provided an analytical model to calculate the bending deformation of conventional hexagonal honeycombs. Alderson et al. [16] has investigated the bending behaviour of 3-coordinated ligament and cylinder-ligament honeycombs using finite element (FE) simulations. Chen has performed a thorough investigation about the bending of conventional hexagonal honeycombs and also found that the Kirchhoff hypothesis underpinning the calculation of the flexural stiffness derived from the homogenized membrane (in-plane) properties of the honeycomb cannot be used to evaluate the out-of-plane bending performance [24,25].

The Authors have previously proposed a ZPR cellular configuration made by combinations of hexagons and thin plates for large out-of-plane morphing capabilities and separate tailorable in-plane and out-of-plane elastic constants, however only the in-plane mechanics have been investigated yet [26]. In this work, the bending performance of this particular configuration is investigated by using analytical models benchmarked with FE simulations and experimental cantilever and 3-point bending tests. A comparison of the out-of-plane experimental bending performance of six different types of cellular structures with positive, zero and negative Poisson's ratio and same relative density has also been performed via three-point bending tests. The sensitivity of the equivalent bending modulus of the ZPR lattice versus its geometric parameters has also been investigated by parametric analyses using a combination of analytical computations and FE homogenization techniques.

* Corresponding authors.
E-mail address: f.scarpa@bristol.ac.uk (F. Scarpa).

http://dx.doi.org/10.1016/j.compstruct.2016.05.078
0263-8223/

2. Models and experimental tests

2.1. Geometry of the honeycomb

The cellular topology features a new mechanism to achieve ZPR, which consists in inserting a hexagonal part to sustain the out-of-plane compression and to produce in-plane compliance with the connection to a thin plate for the large out-of-plane flexibility. Fig. 1 shows the representative unit cells of the lattice with internal cell angles $\theta \geqslant 0°$ and $\theta < 0°$. The length of the inclined and vertical walls are represented by the parameters l and $h = \alpha l$, respectively. The thickness of the hexagon, thin plate and the whole honeycomb are represented by the quantities $t = \beta l$, $b_1 = \lambda b$ and b. The dimension $l_1 = \eta l$ represents the length of the thin plate. The parameter $b = \gamma l$ is used to normalize all dimensions. The width of the unit cell is $w = \alpha l + 2l\sin(\theta)$ for the case of $\theta \geqslant 0°$, while this value becomes $w = \alpha l$ when $\theta < 0°$.

2.2. Analytical models

The calculation of the equivalent bending modulus E_b, is based on an analytical model of the unit cell under pure bending as shown in Fig. 2(a). Because of vertical and horizontal symmetry, the analytical model has been simplified into a quarter model with a fixed end and a free end loaded with an uniformly distributed bending moment **M**, as shown in Fig. 2(b) and (c). No displacement along the 2-direction on the bottom and top surfaces is also present because of symmetry (Fig. 2(b)). For convenience, the quarter model has been separated into 3 sections (Fig. 2(b), (c)). The deformation induced by Section 2 has been neglected because of its significant cross section and shorter length compared with the other 2 sections, acting therefore as a rigid body during bending. One can separate this model therefore into a bending and torsion combined plate (Section 1) and a partly fixed cantilever beam with relatively large width (Section 3). For honeycomb structures, the thickness of the cell wall is usually much smaller than the length and height of the cell wall itself, further justifying the simplification adopted for Section 1 (plate rather than beam). The total deformation of the quarter model is therefore the sum of the deformations from Sections 1 and 3.

The boundary conditions for Sections 1 and 3 are shown in Fig. 3 (a) and (b) respectively. For Section 1, the moment **M** can be resolved into a bending moment M_b and a torsional moment M_t:

$$M_b = M\cos\theta \tag{1}$$

$$M_t = M\sin\theta \tag{2}$$

Through standard engineering beam theory one can generate the bending angle around the 1-direction induced by M_b:

$$\theta_{1b} = \frac{M_b l}{E_s I_1}\cos\theta \tag{3}$$

In (3) E_s is the Young's modulus of the honeycomb material and I_1 the second moment of area of the cross section of the inclined wall. In order to calculate the deformation induced by the torsional moment M_t a torsional coefficient q has been introduced, as follows:

$$\theta_{1t} = \theta_t \sin\theta = \frac{qM_t l}{KG_s}\sin\theta \tag{4}$$

In (4), K is the polar moment of inertia of a solid rectangular section [27] and G_s the shear modulus of the cellular structure. For the inclined wall, one can calculate K by [27]:

$$K = \frac{1}{16}\gamma\beta^3 l^4\left(\frac{16}{3} - 3.36\frac{\beta}{\gamma}\left(1 - \frac{\beta^4}{12\gamma^4}\right)\right) \tag{5}$$

Finite element simulations using the commercial FE code ANSYS 13.0 have been performed to obtain the torsional coefficient q, which represents the ratio between the torsional angles from the FE results and the analytical value, i.e. $q = \theta_{FEM}/\theta_{analytical}$ ($\theta = Tl/(KG)$ [27]). SOLID 45 elements with 8 nodes and three translational degrees have been used in the simulations. The FE model had parametric dimensions of length l_1, height h_1 and thickness t_1 and minimum element size of $t_1/5$ (Fig. 3(c)). Earlier research has shown that the torsional coefficient of a thin plate can be effected by only two factors: the Poisson's ratio υ and the ratio between length and height h_1/l_1 [24]. In these simulations the dependence of the torsional coefficient versus varying Poisson's ratios and different height/length ratios has been investigated. All the nodes on the surface B have been coupled with a master node built at the center of the surface using the MPC 184 element. The torsional moment was then applied on the master node and all three translational degrees of the nodes on the surface A have been constrained while the surfaces C, D, E, F were set with a free boundary. The torsional angle was calculated using the average nodal rotation on the loading surface. Fig. 4 shows the variation of the coefficient q versus different height to length ratios and Poisson's ratios of the core substrate for $l_1 = 10$ mm and $t_1 = 1$ mm. Within the interval of parameters used in the simulations, the value of the coefficient q ranges between 0.23 and 0.95. The total angular deformation of Section 1 around the 1-direction corresponds to the sum of the angles induced by the bending moment M_b and the torsional moment M_t:

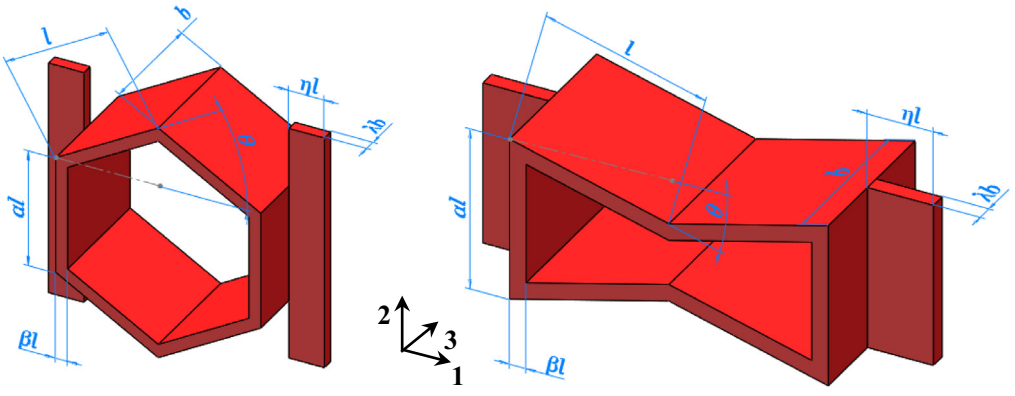

Fig. 1. Geometry of the ZPR configuration with cell angle $\theta \geqslant 0$ (left) and $\theta < 0$ (right) (Redrawn from[26]).

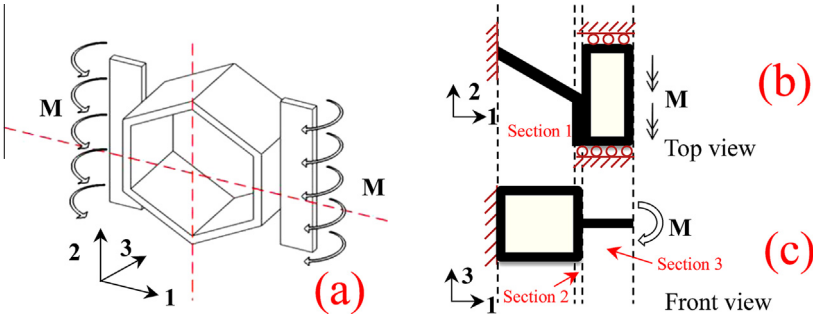

Fig. 2. Schematics of the analytical model used to calculate the equivalent bending modulus.

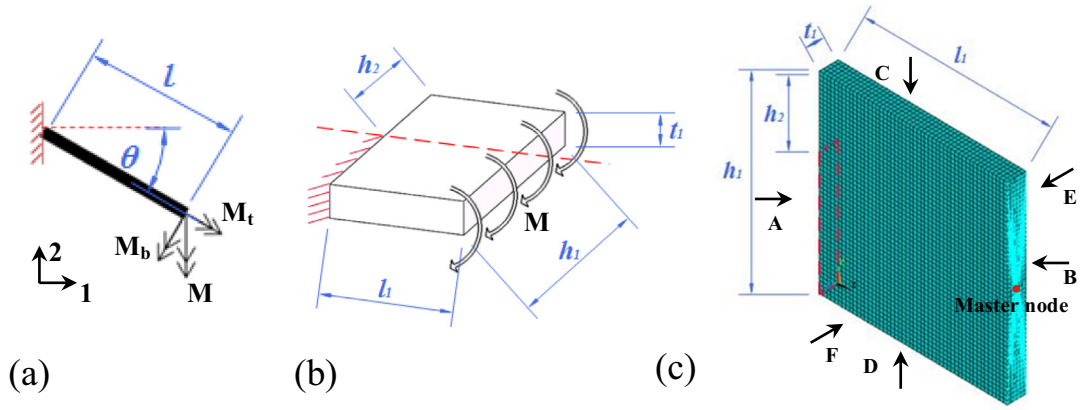

Fig. 3. Models for Section 1 (a) and Section 3 (b), and the FEM grid (c).

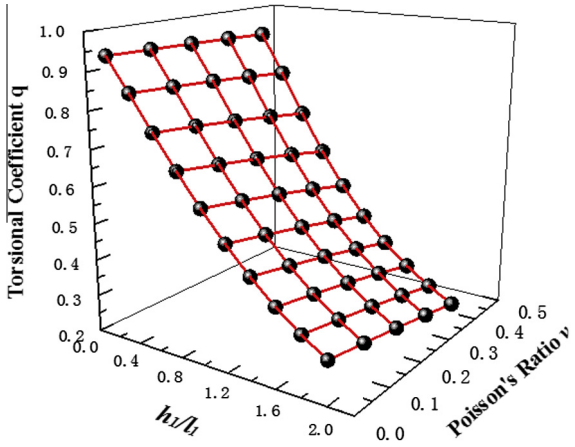

Fig. 4. The torsional coefficient q vs varying height/length and Poisson's ratios.

$$\theta_1 = \theta_{1b} + \theta_{1t} \tag{6}$$

To cater for the deformation occurring in Section 3, that part of the unit cell has been simplified into a sliding cantilever beam with relatively large width (Fig. 3(b)). The cantilever beam has dimensions of length l_1, height h_1, thickness t_1 and the height of the free part of the fixed end is h_2. A parameter μ has been introduced to replace the ratio between the heights of the sliding part and the whole of the fixed end, i.e. $\mu = h_2/h_1$. Because of the existence of the slide in the fixed end, the deformation of the partly fixed cantilever beam with a relatively large width shown in Fig. 3(b) has an intermediate value between the ones of the totally fixed cantilever beams with height of h_1 and $h_1 - h_2$ under the same loading conditions, which have been set as θ_{min} and θ_{max} respectively:

$$\theta_3 = \theta_{\min} + f(l_1, h_1, t_1, \mu)(\theta_{\max} - \theta_{\min}) \tag{7}$$

$$\theta_{\min} = \frac{Ml_1}{\left(\frac{E_s}{1-\upsilon^2}\right)I_2} \tag{8}$$

$$\theta_{\max} = \frac{Ml_1}{\left(\frac{E_s}{1-\upsilon^2}\right)(1-\mu)I_2} \tag{9}$$

In (7)–(9), $f(l_1, h_1, t_1, \mu)$ is a function of four parameters, with υ being the Poisson's ratio of the material and I_2 the second moment of area of the cross section. As the beams have a relatively large width, the bending stiffness has been taken into account by using the Kirchhoff plate formula $E_s/(1-\upsilon_s^2)$ rather than E_s [27]. FEM simulations using the ANSYS 13.0 code have been again performed to derive the function $f(l_1, h_1, t_1, \mu)$. The models consisted in SOLID 45 elements with 8 nodes and three translational degrees, with all nodes on the surface B being coupled to the master node built at the center of the surface using the MPC 184 element (Fig. 3(c)). After a convergence test a minimum element size of $t_1/5$ has also been used during the simulations. The bending moment was applied to the master node. All three nodal translational degrees of freedom in the red dashed rectangle on the surface A (Fig. 3(c)) have been constrained, while the other part on the surface A and the surfaces C, D, E, F were set with free boundaries. The bending angle was also calculated using the average nodal rotation on the surface B. A polynomial fitting over 448 configurations of the partly fixed cantilever beam considered in the cell provides an estimation of the function f ($R^2 = 0.9998$):

$$\begin{aligned} f(l_1,h_1,t_1,\mu) &= (-0.01343 + 0.00154l_1 - 7.85534\times10^{-5}l_1^2 + 1.46685\times10^{-6}l_1^3) \\ &\times(-1.14900 - 1.13647h_1 + 0.01153h_1^2 - 8.00226\times10^{-5}h_1^3) \\ &\times(-2.16699 - 0.11911t_1 - 0.33487t_1^2 + 0.12298t_1^3) \\ &\times(-4.21151\mu + 1.68656\mu^2 + 1.81367\mu^3) \end{aligned} \tag{10}$$

Eq. (10) has been generated within the interval $0 \leqslant \mu \leqslant 0.6$. Substituting Eqs. (8)–(10) and the geometric parameters of the unit cell ($l_1 = \eta l$, $h_1 = \alpha l/2 + l\sin\theta$, $t_1 = \lambda b$, $\mu = l\sin\theta/(\alpha l/2 + l\sin\theta)$ *for* $\theta \geqslant 0$, $\mu = 0$ *for* $\theta < 0$) into Eq. (8), one can obtain the bending angle θ_3 of Section 3.

The total bending angle of the quarter model around the 1 direction is a linear superposition of the type:

$$\theta_b = \theta_1 + \theta_3 \tag{11}$$

The equivalent bending modulus can be therefore calculated as:

$$E_b = \frac{M(\eta l + l\cos\theta)}{\left(\frac{1}{1-\upsilon_{31}^2}\right)\theta_b I_b} \tag{12}$$

In (12), the bending stiffening effect has also been taken into account. The parameter υ_{31} is the out-of-plane Poisson's ratio, which can be considered equal to the one of the solid itself, i.e. $\upsilon_{31} = \upsilon_s$ [1]. I_b is the homogenized second moment of area of the cross section, and could be calculated as:

$$I_b = \begin{cases} \frac{\left(\frac{1}{2}\alpha l + l\sin\theta\right)(\gamma l)^3}{12} & \textit{for } \theta \geqslant 0 \\ \frac{\alpha l(\gamma l)^3}{24} & \textit{for } \theta < 0 \end{cases} \tag{13}$$

2.3. Finite element simulations of the bending modulus

The numerical homogenization of the equivalent bending modulus was performed by using the commercial finite element software ANSYS (version 13.0, ANSYS Inc.). The FEM model was developed using 3D structural elements SOLID 45 with 8 nodes and three translational degrees at each node. The full-size representative volumes used to simulate the bending performance of the hexagons and thin plates combined zero Poisson's ratio honeycomb were given by 6×4 unit cells as shown in Fig. 5. A minimum element size of $t/2$ was used in the simulations according to convergence tests. All degrees of the nodes on the surface A have been constrained and 4 forces were loaded at the center of each unit cell on the surface B. All the other 4 surfaces have been set as free boundaries. The equivalent bending modulus was calculated using the average displacement of the nodes along the 3-direction on the surface B:

$$E_b = \frac{4FL^3}{3wI_b} \tag{14}$$

In (14), F is the loading force on each unit cell, w the average displacement along the 3 direction of the nodes on the surface B, L and I_b the total length and the second moment of area of the cross section of the representative volume respectively. A slenderness ratio of more than 12 has been used in the simulations to guarantee the Euler–Bernoulli beam assumptions that underpin Eq (14).

2.4. Experimental tests

All honeycomb samples used in this paper have been manufactured using ABS plastics with a rapid prototyping Fusion Deposition Molding (FDM) machine (Stratasys Inc., USA). The elastic properties of the ABS plastic have been determined by dog-bone specimens according to the standard test method (ASTM D638-08) in our last work [26].Equivalent isotropic properties ($E_s = 2129$ MPa, $\upsilon_s = 0.42$, $G_s = 749$ MPa) have been obtained using the geometric average value of the orthotropic mechanical properties ($E_x = 2069.5$ MPa, $\upsilon_{xy} = 0.38$, $E_y = 2189.5$ MPa, $\upsilon_{yx} = 0.46$) which were generated from the standard tests [14]. For simplicity, the equivalent isotropic constants have been used in the FEM simulations and the theoretical analysis.

The equivalent bending modulus of the ZPR cellular configuration presented in this work has been evaluated by developing a cantilever beam experimental testing using weights to create a point load at the center of the free end (Fig. 6). A clamp and a holder have been used to produce a fixed end for the samples as shown in Fig. 6(a). A magnet was also used to stabilize the ruler

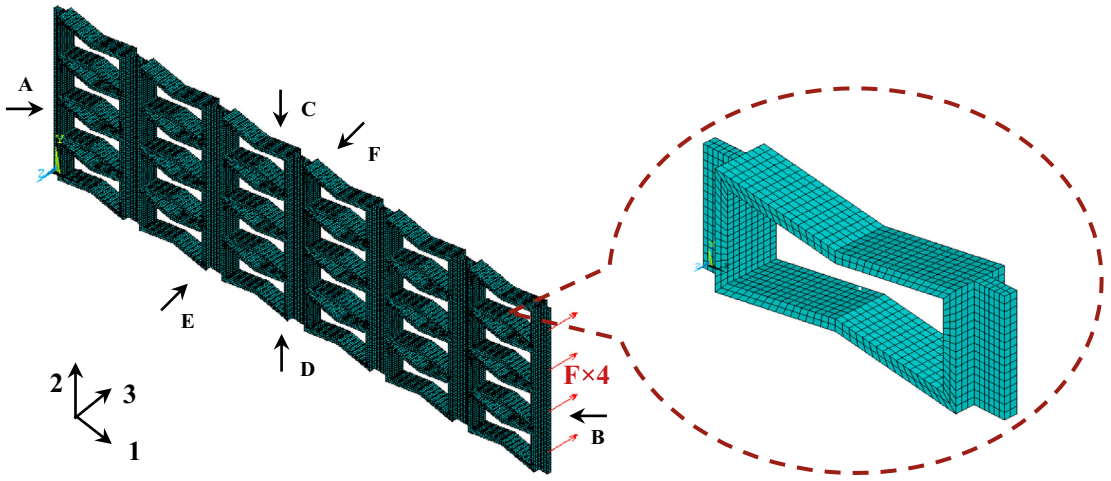

Fig. 5. Finite element model used to calculate the equivalent bending modulus.

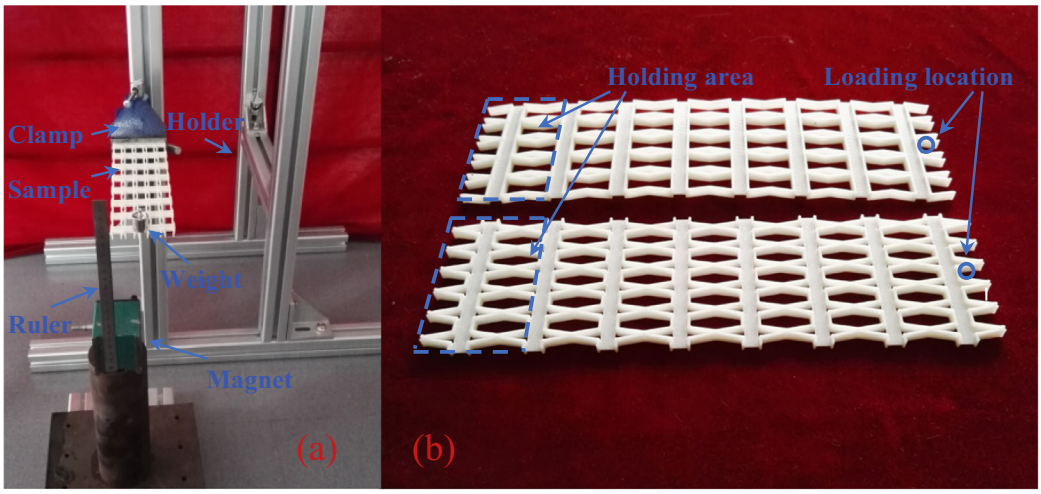

Fig. 6. Experimental setup adopted for the measurement of equivalent bending modulus (a), and the samples used in the experimental tests (b).

that was employed to obtain the displacement of the free end. During the tests a gradienter has been used to control the position of relative the clamp and the ruler (horizontal and vertical respectively). The clamp area and the loading location are shown in Fig. 6 (b). The samples used in these tests have all the same dimensions (200 mm × 60 mm × 4 mm) with at least 5 complete unit cells on the width and more than 7 on the length. Weights of 5 g, 10 g, 20 g, 50 g, 100 g have been used in the tests. The equivalent bending modulus has been calculated from Eq. (14), this time considering as *4F* the whole loading weight force.

A three-point bending test was also designed to perform a comparison of the out-of-plane bending performance of different types of cellular configurations to benchmark the ZPR lattice. A total of 6 types of honeycombs (Fig. 7) were tested with the same 3P bending setup (Fig. 7(a)). The cellular structures consisted in a conventional hexagonal [28], re-entrant (auxetic) [28], anti-tetrachiral (auxetic) [14], ZPR SILICOMB [15,29,30], and the two novel ZPR lattices, one with a positive and the other with a negative cell angle. All samples had the same dimensions (200 mm × 60 mm × 4 mm) with at least 3 complete unit cells along the width. The 3P bending tests were performed using an Instron 3343 testing machine with a 1KN load cell. A displacement rate of 5 mm/min and a span length of 148 mm were used during the tests, and the tests were stopped when the central point deflection reached 30 mm. As the relative density is one of the most important features for a cellular solid [1] all six types of honeycombs were designed to have the same relative density, as shown in Table 1. The estimates of the relative density in Table. 1 were obtained from calculating the relative volumes of the solid models created using the AutoCAD software. The cellular configurations were also designed to have all the cell ribs along the span direction go undergo the same bending deformation. The length of the cell ribs along the span direction was fixed as 10 mm for all types of honeycombs, except the SILICOMB configuration. And that data for the silicomb was 5.9 mm which makes the length on the span direction of a bending beam consists of two connected ribs 10.9 mm.

3. Results and discussions

The geometry parameters of the honeycombs unit cells used in the experimental cantilever beam tests were $l = 10$ mm, $\alpha = 0.65$, $\beta = 0.1$, $\gamma = b/l = 0.4$, $\eta = 0.25$, $\lambda = 0.25$, $\theta = 10°$ for the bottom one in Fig. 6(b), and $l = 10$ mm, $\alpha = 1.2$, $\beta = 0.1$, $\gamma = b/l = 0.4$, $\eta = 0.25$, $\lambda = 0.25$, $\theta = -10°$ for the top one. Table 2 shows the comparison among the analytical model, the FEM simulations and the experimental tests. The equivalent bending modulus for the honeycomb with the 10° internal cell angle obtained from the cantilever beam tests and the 3P bending tests are 14.43% and 4.41% lower than the

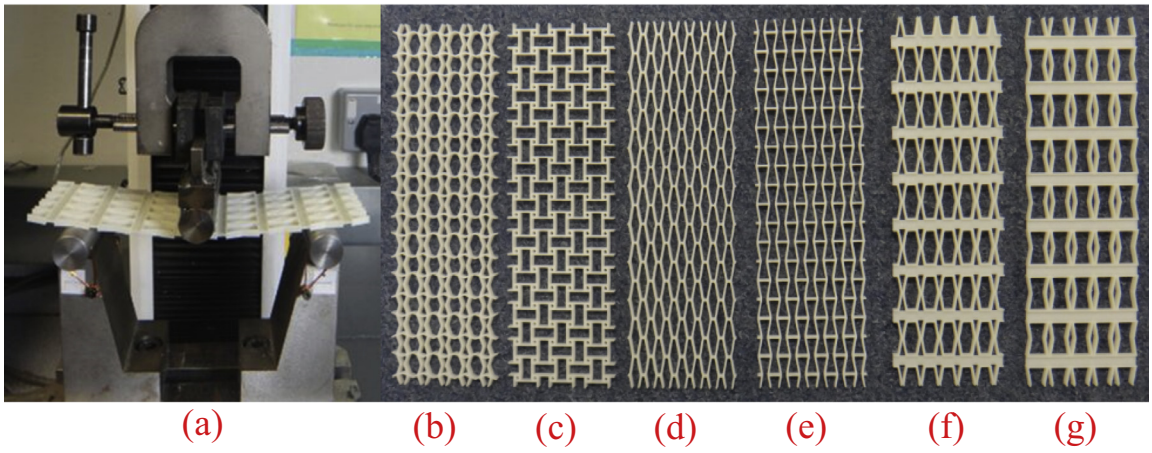

Fig. 7. Experimental setup of the three-point bending tests (a) and the six types of honeycomb used in the tests: (b) SILICOMB; (c) anti-tetrachiral; (d) hexagonal with $\theta = 10°$; (e) re-entrant with $\theta = -10°$; (f) novel ZPR with $\theta = 10°$; (g) novel ZPR with $\theta = -10°$.

Table 1
Relative density of the samples used in three-point bending tests.

Types	SILICOMB	Anti-tetrachiral	Hexagonal with $\theta = 10°$	Re-entrant with $\theta = -10°$	Novel with $\theta = 10°$	Novel with $\theta = -10°$
Relative density	25.6%	25.0%	25.4%	25.7%	25.0%	25.2%

Table 2
Comparison of the analytical, FEM and experimental results.

E_b (MPa)	Analytical	FEM	Cantilever beam tests	3P bending tests
Hoenycomb with $\theta = 10°$	103.07	102.58	88.20 ± 2.28	98.52
Honeycomb with $\theta = -10°$	103.36	100.94	93.08 ± 2.01	111.83

one predicted by the analytical model respectively, and also 14.02% and 3.96% lower than the one provided by the FEM simulation. Both the FE and the analytical model predictions are in a very good agreement, with the FE simulations being only 0.48% lower than the theoretical ones. For the honeycomb with the -10° internal cell angle, the experimental results of the cantilever beam tests show a bending modulus 9.95% and 7.79% lower than the analytical and FE results respectively while the results from the 3P bending tests show discrepancies of 8.19% and 10.79% over the analytical and FE results respectively. Again, a very good agreement can be observed between the analytical and FE predictions, with a discrepancy of 2.34% only. The equivalent bending modulus obtained from cantilever beam tests for the honeycombs with 10° and -10° internal cell angle show differences of 10.48% and 16.77% lower than the results of 3P bending tests. The discrepancy between the analytical, numerical and experimental results can be explained by several reasons. Firstly the deformation of the vertical wall (Section 2 in Fig. 2) has been neglected in the analytical calculation, while this part of deformation were taken into account in the FE simulations and experimental tests. The samples manufactured with the FDM technique do not guarantee the validity of assuming an isotropic and homogeneous material existing as a substrate core for the honeycomb because the layerwise deposition of the ABS plastic and the internal porosity [15,31]. From Fig. 6(b) one can observe that the distance between the loading location and the holding area is $2\eta l$ larger than the length of six complete unit cells (ηl is the length of the thin-plate), therefore the length of $(2\eta l + 6L_{cell})$ was used to postprocessed the results of the cantilever beam tests ($L_{cell} = 2\eta l + 2l\cos\theta$ was the length of the unit cell). The distance between the holding area and the effective loading point (center of the loading location) was larger than $(2\eta l + 6L_{cell})$, and that would directly lead to a smaller value of the equivalent bending modulus.

Fig. 8 shows the comparison of the force–deflection curves for the forementioned 6 types of honeycombs generated from the three-point bending tests. The cellular configurations considered are the two novel ZPR used in the cantiliver tests, the hexagonal one [28] with 10° cell angle $l = 10$ mm, $\alpha = 0.35$, $\beta = 0.1$, $\eta = 1$, $\theta = 10°$, the re-entrant (auxetic) [28] with -10° cell angle $l = 10$ mm, $\alpha = 0.8$, $\beta = 0.1$, $\eta = 1$, $\theta = -10°$, the SILICOMB [15,29,30] ($l = 5.8$ mm, $h = 3.2$ mm, $\theta = 20°$, $\varphi = -20°$) and the auxetic anti-tetrachiral one [14] ($r = 2.1$ mm, $L_x = 10$ mm, $L_y = 10$ mm, $L_{ex} = 6.4$ mm, $L_{ey} = 6.4$ mm, $t = 1$ mm). We must reiterate that all these cellular configurations have the same relative density (~25%). When looking at the zero Poisson's ratio configurations one can notice that the novel ZPR show very similar force/displacement characteristics, with a softening response more evident after 20 mm of displacement and continuing monotonically until the maximum displacement applied (30 mm). The SILICOMB configuration follows a similar trend with higher stiffness, however failure occurs for this cellular structure at 23 mm for a load of 7.94 N. Notably, the novel ZPR configuration with the negative internal cell angle is almost 30% stiffer than the one with the correspondent positive angle. It is worth noticing that the two proposed ZPR configurations and the anti-tetrachiral (auxetic) cellular structure show a higher bending compliance than the other three configurations, as the latter all fail before the deflection reaches 30 mm. The loads for the two novel ZPR and the anti-tetrachiral samples when the deflection is 30 mm are 11.35 N, 12.77 N and 16.78 N, meaning that that the load of the anti-tetrachiral configuration is 47.8% and 31.4% higher that of proposed ZPR lattices with 10°and −10°, respectively. Incidentally, it is worth noticing the behaviour of the re-entrant cellular structure: although its peak load is only 0.31% over the one of the hexagonal structure, the displacement at failure is 60.11% higher than the one exhibited by the hexagonal configuration after following a quasi elasto-plastic behaviour. Considering all six types of honeycombs, the novel ZPR lattices need a smaller load to reach the same deflection. For example, when the deflection is 10 mm, the loads are 22.53 N for the hexagonal

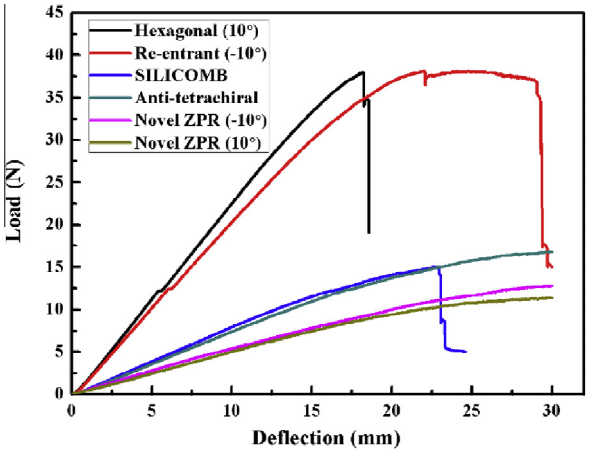

Fig. 8. Load–deflection curves generated from three-point bending tests.

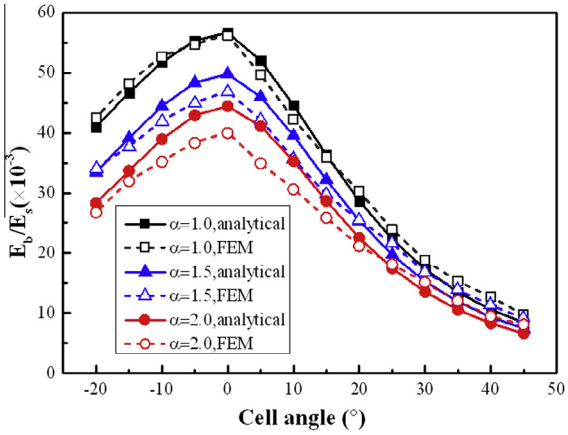

Fig. 9. FE homogenization and analytical predictions of the non-dimensional equivalent bending modulus E_b/E_s versus the cell angles for various parameters α and $\beta = 0.1$, $\eta = 0.25$, $\gamma = 0.4$, $\lambda = 0.25$.

honeycomb, 20.31 N for the re-entrant one, 7.94 N for the SILICOMB and 7.39 N for the anti-tetrachiral. At the same value of the central bending deflection the ZPR with $\theta = 10°$ exhibits a force of 5.01 N and 5.39 N for $\theta = -10°$

4. Parametric analysis

Figs. 9–13 show the variation of the non-dimensional equivalent bending modulus E_b/E_s of the novel ZPR configurationshexagons and thin plates combined honeycomb versus the different geometrical parameters of the unit cell. The theoretical expression of Eq. (12) and the Finite Element simulations have been used to identify the sensitivity of the equivalent bending modulus versus the geometric parameters. During the parametric runs the dimension l was set as a constant (10 mm). From inspecting these figures it is evident that the nondimensional bending modulus reaches a peak at $\theta = 0°$. Decreases of the modulus are evident for $\theta < 0^o$ and $\theta > 0°$, although the sensitivity curves are not symmetric around $\theta = 0°$, and in general the bending modulus is lower for positive internal cell angles. Fig. 9 in particular shows the FE homogenization and analytical predictions of the non-dimensional equivalent bending modulus versus the cell angles for various parameters α and $\beta = 0.1$, $\eta = 0.25$, $\gamma = 0.4$, $\lambda = 0.25$ being constant. From these simulations it is apparent that the simplifying assumption for the analytical model (i.e., neglecting the deformation of the vertical wall) leads to discrepancies against the higher fidelity FE model. The deformation of the vertical wall versus the whole cell deformation increases for increasing dimensions of the vertical wall. An increase of the cell wall aspect ratio α not only leads to a slightly decrease of the equivalent bending modulus, but also to a relatively larger discrepancy between the analytical and the FE results. Fig. 10 also shows that the both of the FE homogenization and the analytical predictions agree on the strong sensitivity of the modulus versus the cell wall thickness aspect ratio β, with an almost 7-times increase of the non-dimensional equivalent bending modulus when the parameter β varies from 0.05 to 0.15 for the structure at $\theta = 30°$. Fig. 11 shows the analogous parametric analysis versus the cell angles for various parameters γ describing the thickness of the honeycomb for a constant thickness of the thin plate ($\lambda\gamma = 0.1$). An increase of the thickness leads to a decrease of the non-dimensional equivalent bending modulus. Figs. 12 and 13 show the sensitivity of the nondimensional bending modulus again versus the cell angles, this time for various parameters (η *and* λ) that describe the length and the thickness of the thin plate respectively. We can observe from Fig. 11 that an increase of the parameter γ results in a relatively large decrease of the equivalent bending modulus E_b/E_s, the latter varying from $\sim 50 \times 10^{-3}$ to $\sim 8 \times 10^{-3}$ when γ shifts from 0.4 to 0.8. However, from Fig. 12

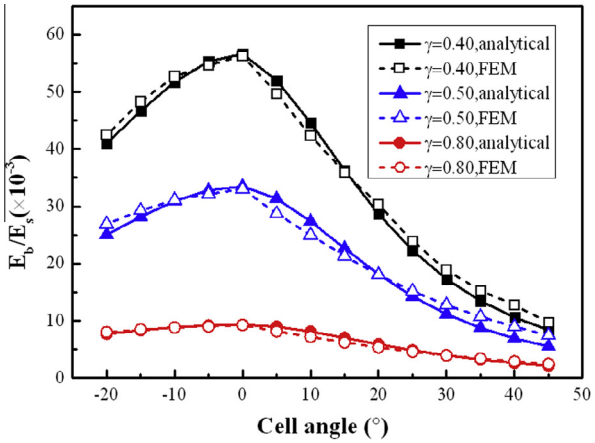

Fig. 11. FE homogenization and analytical predictions of the non-dimensional equivalent bending modulus E_b/E_s versus the cell angles for various parameters γ and $\alpha = 1$, $\beta = 0.1$, $\eta = 0.25$, $\lambda\gamma = 0.1$.

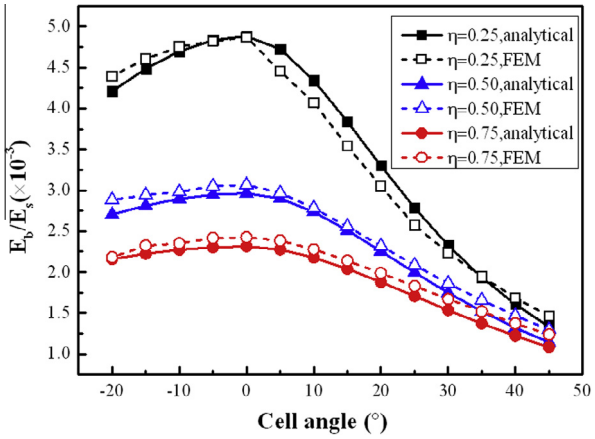

Fig. 12. FE homogenization and analytical predictions of the non-dimensional equivalent bending modulus E_b/E_s versus the cell angles for various parameters η and $\alpha = 1$, $\beta = 0.1$, $\gamma = 1$, $\lambda = 0.1$.

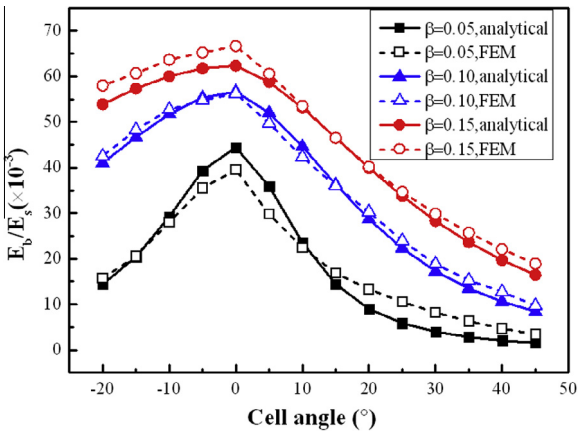

Fig. 10. FE homogenization and analytical predictions of the non-dimensional equivalent bending modulus E_b/E_s versus the cell angles for various parameters β and $\alpha = 1$, $\eta = 0.25$, $\gamma = 0.4$, $\lambda = 0.25$.

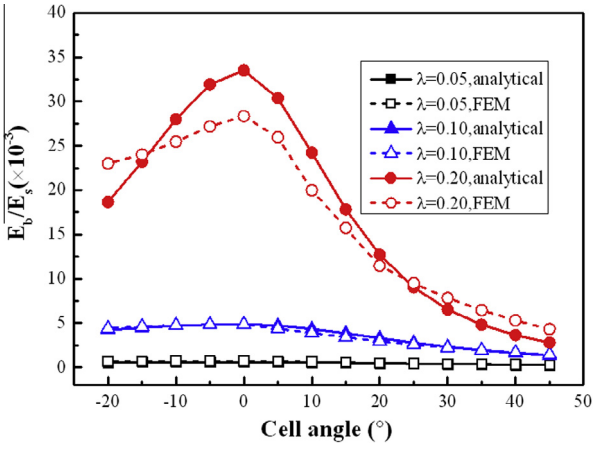

Fig. 13. FE homogenization and analytical predictions of the non-dimensional equivalent bending modulus E_b/E_s versus the cell angles for various parameters λ and $\alpha = 1$, $\beta = 0.1$, $\gamma = 1$, $\eta = 0.25$.

an increase of the parameter η leads to a less significant decrease of the modulus, which makes the parameter γ a suitable choice for the design of the equivalent bending modulus because of its high sensitivity. Another parameter versus which the bending modulus appears to be particularly sensitive is the plate thickness ratio λ (Fig. 13), with more than 3 orders of magnitude of change of the peak bending modulus when passing from $\lambda = 0.05$ to $\lambda = 0.2$. Because a variation of the λ parameter does not induce a change of the single honeycomb cell section and therefore variation of the flatwise compressive properties, the use of this parameter may be an even better choice to tailor the bending performance of the novel ZPR lattice.

5. Conclusions

In this work we have shown the bending mechanical performance of a new class of zero Poisson's ratio lattices designed for large out-of-plane morphing and deformations and separate tailoring of the in-plane and out-of-plane stiffness. These ZPR lattices show an enhanced bending flexibility for large strains, higher than the one exhibited by similar configurations with constant relative density and different Poisson's ratio characteristics. The parametric analyses show that it is possible to obtain large variations and control of the design of the out-of-plane bending performance through the variation of the unit cell geometric parameters. The very large bending compliance of these lattices make them particularly interesting for cellular skin morphing applications involving the use of composite materials.

Acknowledgements

The support of the FP7-AAT.2012.6.3-1-341509 MORPHELLE and the National Natural Science Foundation of China (Grant No.11225211) are gratefully acknowledged. Jian Huang would also thank the British Council and the Chinese Scholarship Council (CSC) for the funding of his research work through University of Bristol.

References

[1] Gibson LJ, Ashby MF. Cellular solids: structure and properties. Cambridge University Press; 1997.
[2] Bitzer T. Honeycomb technology: materials, design, manufacturing, applications and testing. Springer Science & Business Media; 1997.
[3] Scarpa F, Tomlin P. On the transverse shear modulus of negative Poisson's ratio honeycomb structures. Fatigue Fract Eng Mater Struct 2000;23(8):717–20.
[4] Alderson A, Alderson K, Chirima G, Ravirala N, Zied K. The in-plane linear elastic constants and out-of-plane bending of 3-coordinated ligament and cylinder-ligament honeycombs. Compos Sci Technol 2010;70(7):1034–41.
[5] Sun C, Vaidya R. Prediction of composite properties from a representative volume element. Compos Sci Technol 1996;56(2):171–9.
[6] Lira C, Scarpa F. Transverse shear stiffness of thickness gradient honeycombs. Compos Sci Technol 2010;70(6):930–6.
[7] Scarpa F, Panayiotou P, Tomlinson G. Numerical and experimental uniaxial loading on in-plane auxetic honeycombs. J Strain Anal Eng Des 2000;35(5):383–8.
[8] Bezazi A, Scarpa F, Remillat C. A novel centresymmetric honeycomb composite structure. Compos Struct 2005;71(3–4):356–64.
[9] Grima JN, Gatt R, Alderson A, Evans K. On the potential of connected stars as auxetic systems. Mol Simul 2005;31(13):925–35.
[10] Prall D, Lakes R. Properties of a chiral honeycomb with a Poisson's ratio of—1. Int J Mech Sci 1997;39(3):305–14.
[11] Miller W, Smith C, Scarpa F, Evans K. Flatwise buckling optimization of hexachiral and tetrachiral honeycombs. Compos Sci Technol 2010;70(7):1049–56.
[12] Lorato A, Innocenti P, Scarpa F, Alderson A, Alderson K, Zied K, et al. The transverse elastic properties of chiral honeycombs. Compos Sci Technol 2010;70(7):1057–63.
[13] Alderson A, Alderson KL, Attard D, Evans KE, Gatt R, Grima JN, et al. Elastic constants of 3-, 4- and 6-connected chiral and anti-chiral honeycombs subject to uniaxial in-plane loading. Compos Sci Technol 2010;70(7):1042–8.
[14] Chen Y, Scarpa F, Liu Y, Leng J. Elasticity of anti-tetrachiral anisotropic lattices. Int J Solids Struct 2013;50(6):996–1004.
[15] Lira C, Scarpa F, Tai Y, Yates J. Transverse shear modulus of SILICOMB cellular structures. Compos Sci Technol 2011;71(9):1236–41.
[16] Alderson A, Alderson KL, Chirima G, Ravirala N, Zied KM. The in-plane linear elastic constants and out-of-plane bending of 3-coordinated ligament and cylinder-ligament honeycombs. Compos Sci Technol 2010;70(7):1034–41.
[17] Evans K. The design of doubly curved sandwich panels with honeycomb cores. Compos Struct 1991;17(2):95–111.
[18] Lakes R. Foam structures with a negative Poisson's ratio. Science 1987;235(4792):1038–40.
[19] Miller W, Smith CW, Scarpa F, Evans KE. Flatwise buckling optimization of hexachiral and tetrachiral honeycombs. Compos Sci Technol 2010;70(7):1049–56.
[20] Evans K, Alderson K. Auxetic materials: the positive side of being negative. Eng Sci Educ J 2000;9(4):148–54.
[21] Neville R, Monti A, Hazra K, Scarpa F, Remillat C, Farrow I. Transverse stiffness and strength of Kirigami zero-ν PEEK honeycombs. Compos Struct 2014;114:30–40.
[22] Grima JN, Oliveri L, Attard D, Ellul B, Gatt R, Cicala G, et al. Hexagonal honeycombs with zero Poisson's ratios and enhanced stiffness. Adv Eng Mater 2010;12(9):855–62.
[23] Abd El-Sayed FK, Jones R, Burgess IW. A theoretical approach to the deformation of honeycomb based composite materials. Composites 1979;10(4):209–14.
[24] Chen DH. Bending deformation of honeycomb consisting of regular hexagonal cells. Compos Struct 2011;93(2):736–46.
[25] Chen DH. Equivalent flexural and torsional rigidity of hexagonal honeycomb. Compos Struct 2011;93(7):1910–7.
[26] Huang J, Gong X, Zhang Q, Scarpa F, Liu Y, Leng J. In-plane mechanics of a novel zero Poisson's ratio honeycomb core. Compos B Eng 2016;89:67–76.
[27] Young WC, Budynas RG. Roark's formulas for stress and strain. New York: McGraw-Hill; 2002.
[28] Olympio KR, Gandhi F. Flexible skins for morphing aircraft using cellular honeycomb cores. J Intell Mater Syst Struct 2009;21(17):1719–35.
[29] Lira C, Scarpa F, Olszewska M, Celuch M. The SILICOMB cellular structure: mechanical and dielectric properties. Phys Status Solidi B 2009;246(9):2055–62.
[30] Virk K, Monti A, Trehard T, Marsh M, Hazra K, Boba K, et al. SILICOMB PEEK Kirigami cellular structures: mechanical response and energy dissipation through zero and negative stiffness. Smart Mater Struct 2013;22(8):084014.
[31] Bellini A, Güçeri S. Mechanical characterization of parts fabricated using fused deposition modeling. Rapid Prototyping J 2003;9(4):252–64.